

Lagrangian one-particle velocity statistics in a turbulent flow

Jacob Berg*

Risø National Laboratory, 4000 Roskilde, Denmark

(Dated: February 9, 2008)

Abstract

We present Lagrangian one-particle statistics from the Risø PTV experiment of a turbulent flow. We estimate the Lagrangian Kolmogorov constant C_0 and find that it is affected by the large scale inhomogeneities of the flow. The pdf of temporal velocity increments are highly non-Gaussian for small times which we interpret as a consequence of intermittency. Using Extended Self-Similarity we manage to quantify the intermittency and find that the deviations from Kolmogorov 1941 similarity scaling is larger in the Lagrangian framework than in the Eulerian. Through the multifractal model we calculate the multifractal dimension spectrum.

*Electronic address: jacob.berg.joergensen@risoe.dk

I. INTRODUCTION

In the present contribution we present experimental results on Lagrangian one-particle statistics from an experiment with the Risø Particle Tracking Velocimetry (PTV) setup. We focus on small-scale statistics in a turbulent flow: the statistic is analyzed with Extended Self-Similarity (ESS) [2] and the results are presented in the spirit of the multifractal model of turbulence [11]. The use of ESS is discussed together with the multifractal model in a finite Reynolds number flow like the present.

We have performed a Particle Tracking Velocimetry (PTV) experiment in an intermediate Reynolds number turbulent flow. The flow has earlier been reported in [3, 4, 14] although we use data from a recording with a slightly lower Reynolds number. PTV is an experimental method suitable for obtaining Lagrangian statistics in turbulent flows [9, 13, 19, 20, 24, 33]: Lagrangian trajectories of fluid particles in water are obtained by tracking neutrally buoyant particles in space and time. The flow is generated by eight rotating propellers, which change their rotational direction in fixed intervals in order to suppress a mean flow, placed in the corners of a tank with dimensions $32 \times 32 \times 50\text{cm}^3$ (see Fig 1). The data acquisition system

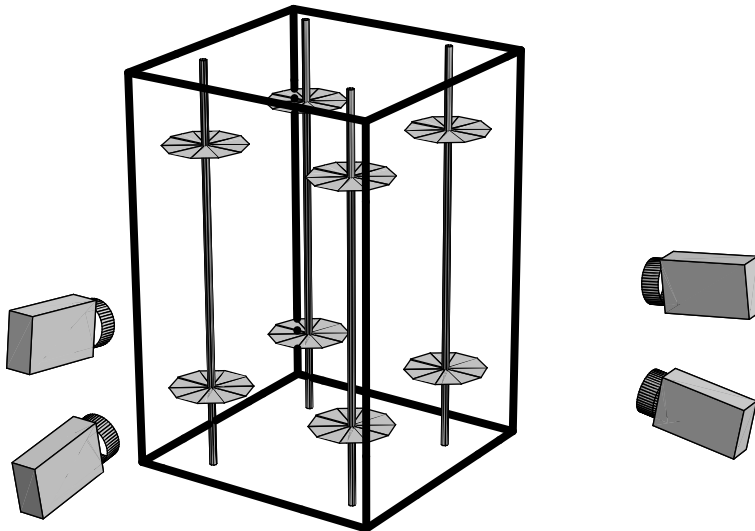


FIG. 1: Experimental setup

consists of four commercial CCD cameras with a maximum frame rate of 50Hz at 1000×1000

η	L	τ_η	T_E	ε	σ_u	Re_λ
0.30mm	53.80mm	0.09s	2.83s	128mm ² /s ³	19.02mm/s	124

TABLE I: Turbulence characteristics: ε is the mean kinetic energy dissipation, $\eta \equiv (\nu^3/\varepsilon)^{1/4}$ is the Kolmogorov length scale with the kinematic viscosity $\nu = 1$ of water. $\tau_\eta \equiv (\nu/\varepsilon)^{1/2}$ is the Kolmogorov time scale and $\sigma_u^2 = \frac{1}{3}(\sigma_{u_x}^2 + \sigma_{u_y}^2 + \sigma_{u_z}^2)$ is the standard deviation of velocity. The integral length scale is defined as $L = \sigma^3/\varepsilon$ while T_E is the eddy turnover time $T_E = L/\sigma_u$. The Reynolds number is defined as $Re_\lambda = \sqrt{15}(L/\eta)^{2/3}$.

pixels. The measuring volume covers roughly (12cm)³. We use polystyrene particles with size $\sim 400\mu\text{m}$ and density very close to one. We follow $\mathcal{O}(1000)$ particles at each time step with a position accuracy of 0.05 pixels corresponding to less than $10\mu\text{m}$.

The Stokes number, τ_I/τ_η (τ_I denotes the inertial relaxation time for the particle to the flow while τ_η is the Kolmogorov time) is much less than one and the particles can therefore be treated as passive tracers in the flow. The particles are illuminated by a 250W flash lamp.

The mathematical algorithms for translating two dimensional image coordinates from the four camera chips into a full set of three dimensional trajectories in time involve several crucial steps: fitting gaussian profiles to the 2d images, stereo matching (line of sight crossings) with a two media (water-air) optical model and construction of 3d trajectories in time by using the kinematic principle of minimum change in acceleration [21, 32].

The flow characteristics are presented in Table I. The mean flow is axisymmetric with a significant vertical straining on the largest scales and we did not find any significant differences from the flow reported in [3, 14], where properties of the mean flow can be found.

Here we look at a sub-volume of the full measuring volume. Only particles which we can observe within a ball of radius 50mm is considered and the turbulence characteristics given in Table I are thus only determined from particles inside this ball. The ball is centered approximately in the center of the tank where the velocity standard deviation σ_u has a global minimum. Inside the ball the particles are uniformly distributed. With $\tau_\eta = 0.09\text{s}$ and a recording frequency at 50Hz the temporal resolution is $\sim 4\text{frames}/\tau_\eta$.

The database is the largest we have compiled and it consists of $\sim 10^6$ individual trajectories with an average length of $\sim 8\tau_\eta$, a standard deviation of $\sim 13\tau_\eta$ and the longest

tracks we find are $\sim 150\tau_\eta$. The number of tracks was an important requirement since the calculation of high order moments is considered important.

Throughout the paper we will denote the *Lagrangian* velocity along a particle trajectory for $\mathbf{v}(t)$ and the *Eulerian* velocity in a fixed frame of reference for $\mathbf{u}(\mathbf{x}, t)$.

II. FINITE VOLUME MEASUREMENTS

A nice property of the Eulerian velocity statistic is that it is stationary in time in the present experiment. This is not the case for the Lagrangian statistics. The non-stationarity

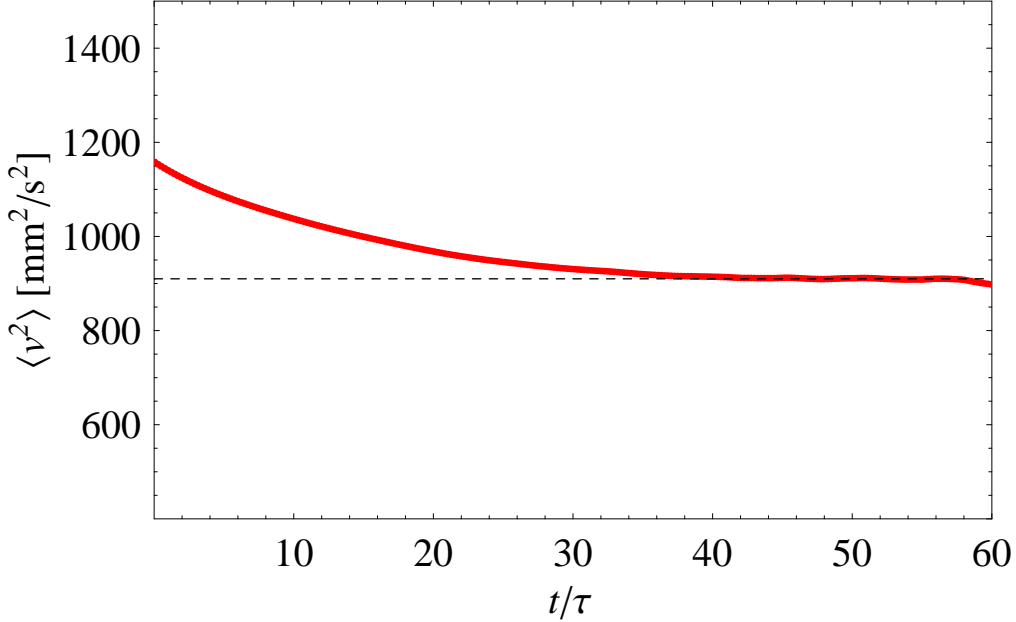


FIG. 2: $\langle v^2(t + t_0) \rangle$. The average is taken over all particles which were observed inside B at both time t_0 and $t_0 + t$.

is showed in Figure 2 where $\langle v^2 \rangle$ is observed to decrease over time. This reflects the finite measuring volume and the non-uniform forcing in space in our experiment: the particles only gain kinetic energy close to the propellers. During their subsequent motion the particles loose kinetic energy until they again come close to the propellers which are constantly spinning. Looking at a finite measuring volume away from the propellers, there will therefore be a flux of kinetic energy into the volume. Inside the volume the kinetic energy is dissipated and

hence we have at the entry of the volume

$$\frac{1}{2} \frac{d}{dt} \langle v^2 \rangle = -\varepsilon, \quad (1)$$

where we recognize the mean kinetic energy dissipation ε . From Figure 2 we find $\varepsilon = 124 \text{mm}^2/\text{s}^2$. This number is close to the number obtained from the second order Eulerian Structure Function $\varepsilon = 132 \text{mm}^2/\text{s}^2$. We take the difference as the uncertainty in estimating ε . Eqn. 1 can also be derived directly from the Navier-Stokes equation by assuming global homogeneity.

The Lagrangian second-order structure function is defined as

$$S_L^2(\tau) = \langle [v(t+\tau) - v(t)]^2 \rangle, \quad (2)$$

where $v(t)$ is here the velocity component along a fluid trajectory. Similar the Lagrangian co-variance function is defined as

$$R_L(\tau) = \langle v(t)v(t+\tau) \rangle. \quad (3)$$

The non-stationarity of $\langle v^2 \rangle$ means that

$$S_L^2(t) = \langle v^2(t) \rangle + \langle u^2 \rangle - 2R_L(t) < 2(\langle u^2 \rangle - R_L(t)), \quad (4)$$

where we have used that the Lagrangian velocity on the boundary of the measuring volume B equals the Eulerian velocity and therefore $\langle v^2(t=0) \rangle = \langle u^2 \rangle$. $S_L^2(t)$ is plotted in Figure 3 for all three velocity components. It is clear that for long times S_L^2 does not approach $2\langle u^2 \rangle$ in agreement with eqn. 4.

A common interpretation of the finite volume influence on Lagrangian statistics is that the particles we can observe for long times are relatively slow ones or particles which are trapped in high intensity vortices (see later). Here we emphasize the equivalence with the energy argument of decaying turbulence described above. Particles which can be observed for long times are slow because it is long time ago they gained kinetic energy at the forcing site.

In Direct numerical simulations (DNS) forcing occurs in wave-number space on the lowest wave-numbers. We therefore have $d\langle v^2 \rangle/dt = 0$ and consequently Lagrangian stationarity. Most physical flows encountered in nature will, however, be Lagrangian non-stationary.

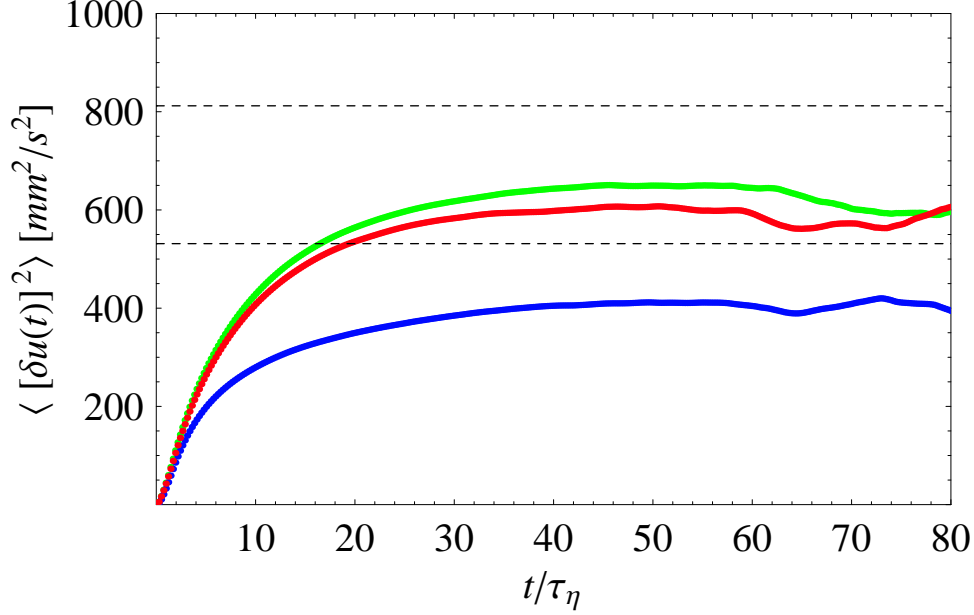


FIG. 3: Second order Lagrangian structure function for the three coordinates of $\mathbf{v}(t)$. x : green (radial component), y : red (radial component) and z : blue (vertical component). The horizontal lines is the Eulerian velocity variance $\langle u^2 \rangle$.

III. ANISOTROPY AND INERTIAL RANGE SCALING

The linear dependence of Re_λ on T_L/τ_η implies that a very high Reynolds number is needed in order to obtain a clear Lagrangian inertial range. Yeung [35] concluded, based on extrapolations from Eulerian fields in DNS, that at least $Re_\lambda \sim 600 - 700$ was needed. Experimental flows at $Re_\lambda = 1000$ [18] and $Re_\lambda = 815$ [22] do, however, not show a very pronounced inertial range defined as a linear regime in the second-order structure function S_L^2 .

In the inertial range $\tau_\eta < \tau < T_L$, K41 similarity theory predicts

$$S_{L,ij}^2(\tau) = C_0 \varepsilon \tau \delta_{ij}, \quad (5)$$

where the Lagrangian Kolmogorov constant C_0 is supposed to be universal for infinite Reynolds numbers [25]. C_0 plays a crucial role in stochastic models [26] and has lately been shown to reflect anisotropy in the large-scale forcing [22]. In Figure 4 we present results of C_0 for the three coordinates of $\mathbf{v}(t)$. According to eqn. 5, C_0 should be determined from a plateau in the inertial range. The parabolic form therefore reflects the almost vanish-

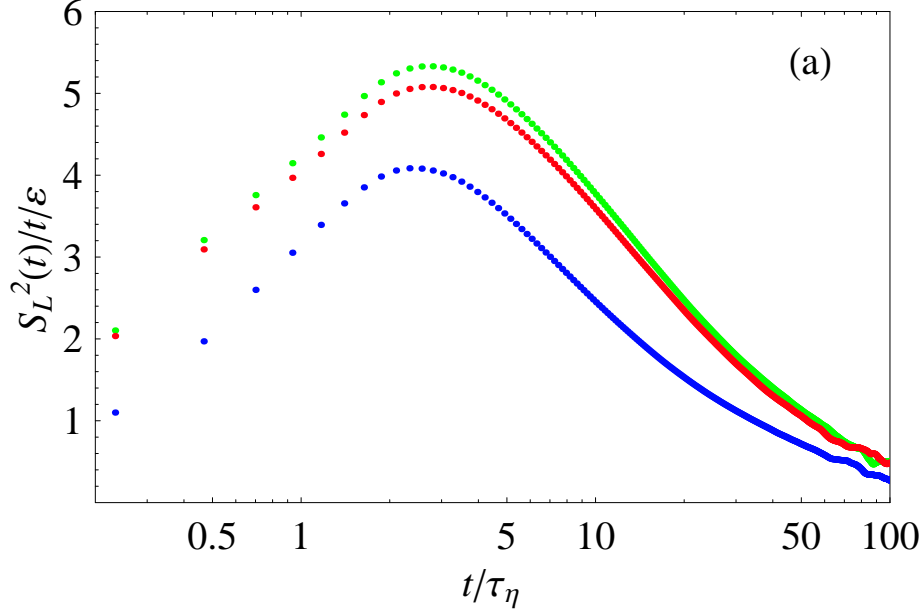


FIG. 4: C_0 for the radial components (green and red) and the axisymmetric component (blue).

ing inertial range in our experiments. The difference between radial and the axisymmetric component stems from the large scale anisotropy. Since C_0 is maximum for times around $2 - 4\tau$ and therefore mainly associated with small scales the difference is a clear signature of small-scale anisotropy. The values of C_0 are 5.34 ± 0.16 , 5.08 ± 0.15 and 4.09 ± 0.12 for the three components x , y and z respectively.

It is interesting to see that the slight difference in the radial forcing is surviving all the way down. The propellers forcing the flow are attached to four rods placed in the corners of the tank. The reason for the radial components being different is probably small differences in the manual vertical placement of the propellers on the rods. The lack of small-scale isotropy in the current experiment should not be taken as a failure of Kolmogorov's hypothesis of local isotropy. For that the Reynolds number is not high enough. Other experiments at much higher Reynolds number do, however, all indicate that the large scale inhomogeneities are also present at smaller scales although with smaller amplitude [22, 28, 29].

Alternatively one can calculate the lagrangian velocity spectrum $\Phi(\omega)$ and calculate C_0 from this. $\Phi(\omega)$ is defined as the fourier transform of the velocity co-variance function $R_L(\tau)$ [31]:

$$\Phi(\omega) = \frac{1}{2\pi} \int_{-\infty}^{\infty} d\tau \exp(-i\omega\tau) R_L(\tau). \quad (6)$$

In the inertial range K41 predicts

$$\Phi_{ij}(\omega) = \beta \varepsilon \omega^{-2}, \quad (7)$$

with $C_0 = \pi\beta$. In Figure 5 (a) we have plotted $R_L(t)$ in the three directions. The radial components fall off exponential with e-folding times $T_{exp}^x \sim 10.7\tau_\eta$ and $T_{exp}^y \sim 9.4\tau_\eta$ while the vertical axisymmetric component $T_{exp}^z \sim 14\tau_\eta$. Since $R_L(\tau)$ is composed of eddies of all size in the flow, the energy containing scales and hence the large scale inhomogeneities strongly effects its form. The integration of $R_L(t)/\sigma^2$ gives the Lagrangian integral time scale T_L . We find values of $T_L \sim T_{exp}$. The velocity spectrum $\Phi(\omega)$ is shown in (b). For

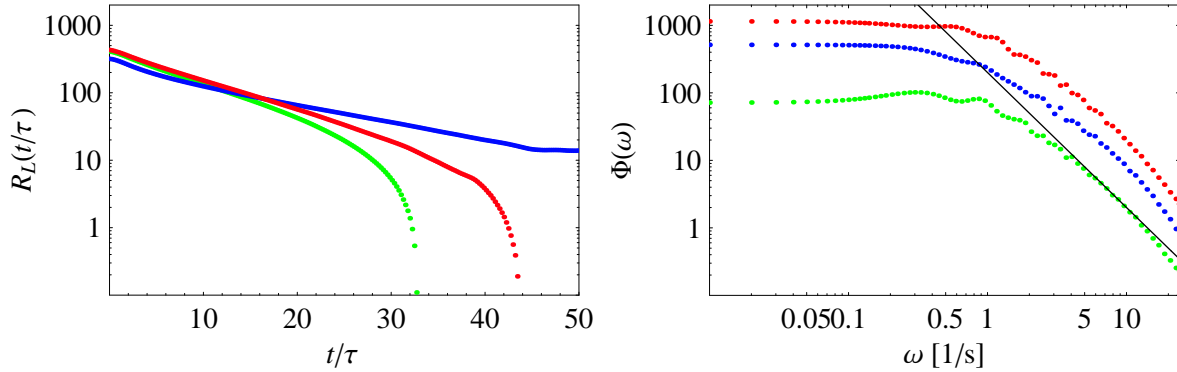


FIG. 5: (a) $R_L(\tau)$. (b) $\Phi(\omega)$. The straight line is the K41 prediction $\sim \omega^{-2}$. Color codes as in Figure 4. The curves have been shifted vertically for clarity.

small frequencies ω the spectrum for all three components are white. This corresponds to uncorrelated velocities for long time lags on a track. For higher frequencies all three spectra turn red with slope of ~ -2 in agreement with the Kolmogorov prediction. Due to a relative low sampling rate ($dt = 0.021s$) the Nyquist frequency prevent us from studying frequencies higher than $\omega = 23.8s^{-1}$.

Lien and D'Asaro [12] studied the scaling properties in a simple Lorentzian model spectrum and found that with a finite Reynolds number it is easier to obtain inertial range scaling from the spectrum than from the structure function $S_L^2(\tau)$. We have plotted the spectrum compensated with ω^2 in Figure 6 in order to have a better look at the existence of an inertial range. For all three components a narrow inertial range is observed as a plateau. The

horizontal lines are used for estimating C_0 . We find values equal to 4.91 ± 0.15 , 4.79 ± 0.14 and 4.07 ± 0.12 for the three components respectively. These values are smaller and a bit more isotropic than those calculated from the structure functions. This is in contrast to the arguments by Lien and D’Asaro [12] C_0 who state that they should be larger.

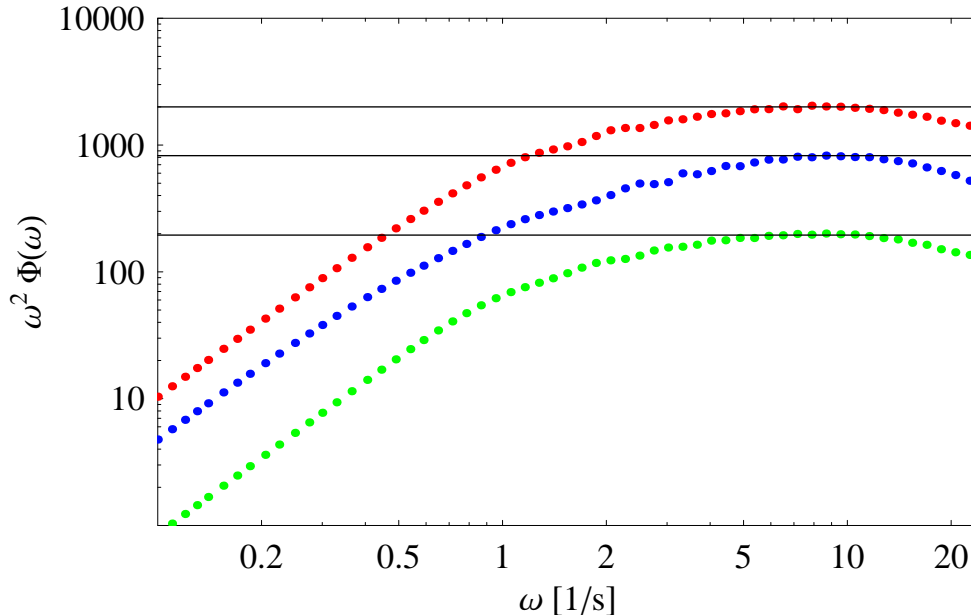


FIG. 6: Compensated velocity spectrum $\omega^2\Phi(\omega)$. Color code as in Figure 4. The curves have been shifted vertically for clarity. One can therefore not determine the magnitude of $\omega^2\Phi(\omega)$ from the different curves. The horizontal lines are the levels from which C_0 is calculated.

IV. SMALL-SCALE INTERMITTENCY

From the study of the lower moments we proceed to higher order moments describing the most extreme events.

The pdfs of temporal velocity increments $\delta v(\tau) = v(t + \tau) - v(t)$ are shown in Figure 7 for different time lags τ . All three components are shown. The three components show the same over all behavior: for large time lags the distributions are Gaussian while they for small time lags have fat tails. The curves corresponding to the smallest time lags have a flat plateau at $\delta v \sim 0$. This is a binning artifact and does therefore not represent any physical trend in the data. The non-Gaussianity for small times becomes more clear by looking at the flatness. The flatness of the distributions is defined as

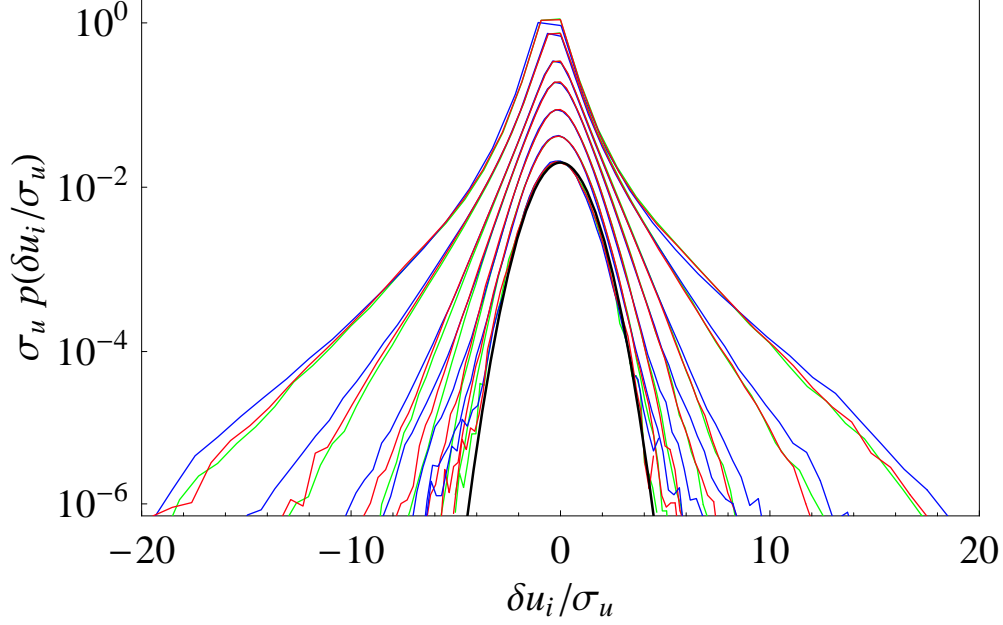


FIG. 7: pdf of velocity increments $\delta v(\tau)$ for times (decreasing downwards) $\tau = 1.0\tau_\eta, 1.7\tau_\eta, 3.6\tau_\eta, 6\tau_\eta, 12\tau_\eta, 24\tau_\eta$ and $48\tau_\eta$. The curves have been shifted vertically for clarity. Color coding as in Figure 4. The black curve is a Gaussian.

$$F(\tau) \equiv \frac{\langle \delta v^4(\tau) \rangle}{\langle \delta v^2(\tau) \rangle^2} \quad (8)$$

and is shown in Figure 8. F is monotonically decreasing for all three components and reaches a Gaussian level at time lags: $\tau \sim 40\tau_\eta$, which is substantial larger than T_L . We do not at present have any explanation for this.

The results presented in Figure 7 and 8 are strong evidence of Lagrangian intermittency, i.e. non-Gaussian behavior of the smallest temporal scales in the flow. These results agree with observations by Mordant et al. [19] and Direct Numerical Simulations (DNS) by Biferale et al. [6].

Our findings suggest that intermittency can be studied in flows with a moderate Reynolds number of order $\mathcal{O}(100)$. The only necessary condition seems to be the size of the ensemble: a large number of particles is needed to observe rare events.

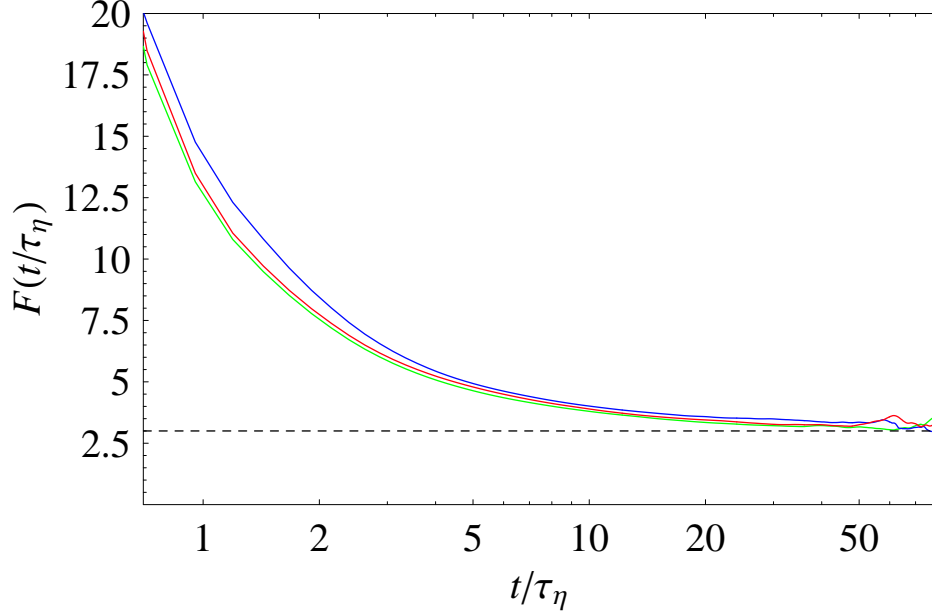


FIG. 8: The flatness of $\delta v(\tau)$. The color coding as in Figure 4. The horizontal line $F = 3$ is the Gaussian prediction.

A. Higher order structure functions and ESS

Before we look at the higher order moments we check for convergence of these. In Figure 9 we show $\delta v^n(\tau)p(\delta v(\tau))$ for $n = 4, 6, 8, 10$. The time lag in all four plot is $\tau = 2.1\tau_\eta$. For $n < 8$ we observe convergence. For $n = 8$ we start to get into trouble, but it seems like we have captured most of the signal – at least for the radial components (red and green curves). In an incompressible flow $\langle \delta u(\tau) \rangle = 0$: the non-zero skewness observed in all the curves is therefore an artifact of sampling errors and / or tracking of particles. This is an issue which has to be resolved before more dramatic conclusions can be made.

K41 similarity theory predicts in the inertial range for the p order structure function:

$$S_L^p(\tau) \equiv \langle \delta v^p(\tau) \rangle \sim \varepsilon^{p/2} \tau^{p/2}. \quad (9)$$

Intermittency can be defined as the departure from K41 similarity scaling. This means that eqn. 9 can be replaced by a more general form taking intermittency into account:

$$\langle \delta v^p(\tau) \rangle \sim \tau^{\zeta_p^L}, \quad (10)$$

where ζ_p^L is commonly named the Lagrangian anomalous scaling exponent. Only recently it has been possible to measure ζ_p^L and hence quantitatively describe the extreme dynamics

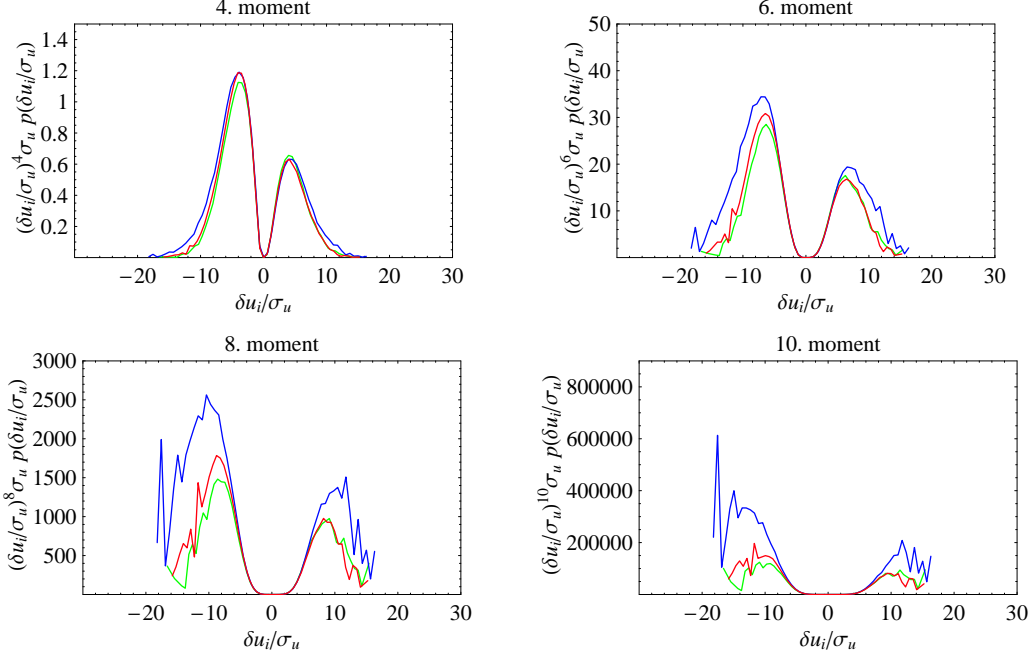


FIG. 9: $\delta v^n p(\delta v)$ for $n = 4, 6, 8, 10$. The time in all four plot is $\tau = 2.1\tau_\eta$.

present in the fat tails of the distribution of $\delta v(\tau)$ for $\tau \rightarrow 0$ [5, 18, 19, 33, 34]. The data presented here is therefore merely a verification of already obtained results.

In Figure 10 (a) structure functions $S_L^p(t)$ of order $p = 2, 4, 5, 6, 8$ are shown as a function of τ . Power laws have been fitted to each function in the region $2\tau_\eta \leq t \leq 4\tau_\eta$ corresponding to the maxima of $S_L^p(t)/t/\varepsilon$. The fits are not convincing. First of all, the inertial range is too narrow and we therefore can not expect any universal scaling. Secondly, and less importantly, we know that the small scales are affected by the large-scale inhomogeneities.

A popular way of looking at scaling exponent is instead to measure ratios of scaling exponents. This method is called Extended self-similarity (ESS) and was introduced by Benzi et al. [2]. The method was introduced in the Eulerian frame but can be transferred to the Lagrangian frame if we assume that $\zeta_2^L = 1$ following K41 similarity theory. The crucial step is to treat all velocity increments as positive. This affects the odd-numbered structure functions. We therefore define

$$S_{L,ESS}^p(\tau) \equiv \langle |\delta v(\tau)|^p \rangle \sim \langle \delta v^2(\tau) \rangle^{\zeta_p^{L,ESS}}. \quad (11)$$

In Figure 10 (b) $S_{L,ESS}^p(t)$ is shown as a function of $S_L^2(t)$. The scaling is now much better, which explains the wide popularity of the method. The different scaling exponents are

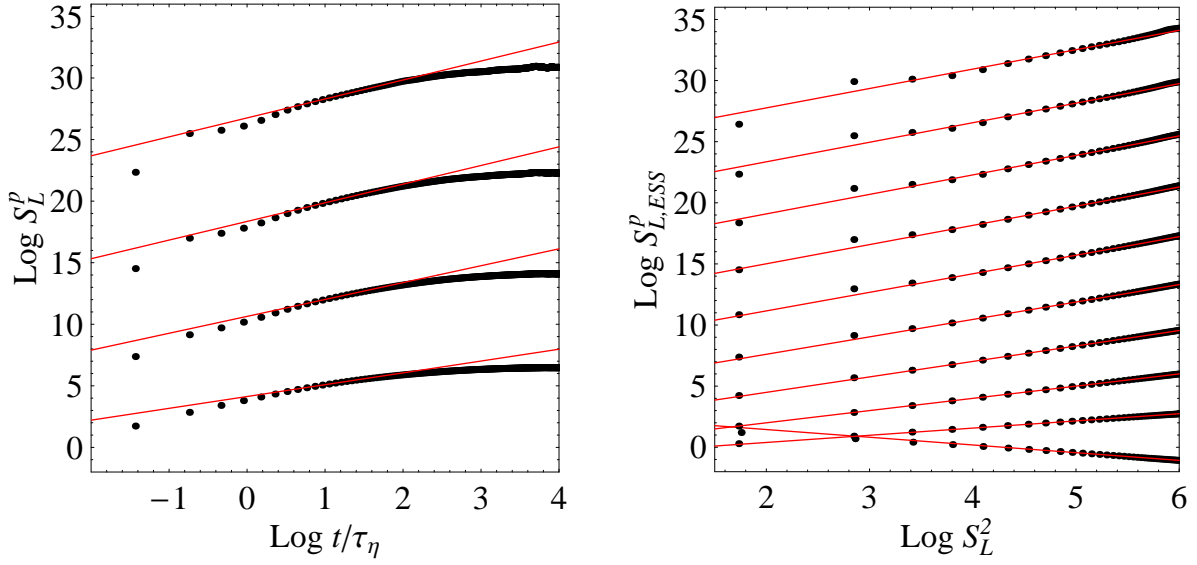


FIG. 10: (a) $S_L^p(t)$ as a function of t/τ_η for $p = 2, 4, 6, 8$ increasing upwards. (b) Extended self-similarity: $S_{L,ESS}^p(t)$ as a function of $S_L^2(t)$ for $p = -1, 1, 2, \dots, 9$. In both panels data from the radial x -component are used.

p	-1	1	2	3	4
ζ_p^L	—	—	0.98 ± 0.07	—	1.40 ± 0.08
$\zeta_p^{L,ESS}$	-0.62 ± 0.07	0.59 ± 0.02	1	1.27 ± 0.03	1.43 ± 0.06
p	5	6	7	8	9
ζ_p^L	—	1.56 ± 0.10	—	1.66 ± 0.17	—
$\zeta_p^{L,ESS}$	1.53 ± 0.05	1.60 ± 0.06	1.65 ± 0.09	1.70 ± 0.13	1.75 ± 0.19

TABLE II: Lagrangian anomalous scaling exponents

printed in Table II and plotted in Figure 11 for the radial components. The error bars represent small deviations between the two radial components as well as an error estimated from fitting the straight lines in Figure 10. The errors increase with p and are significantly larger for ζ_p^L compared to the ESS approach $\zeta_p^{L,ESS}$.

Some remarks about ESS should be made at this point. In the original paper Benzi et al. [2] argued, based on experimental evidence of $|\langle \delta_r u^3(r) \rangle| \sim \langle |\delta_r u(r)|^3 \rangle$, that $\langle |\delta_r u(r)|^p \rangle = B_p \langle |\delta_r u(r)|^3 \rangle^{\zeta_p^{E,ESS}}$. As also emphasized in the paper this is not a rigorous result which can be

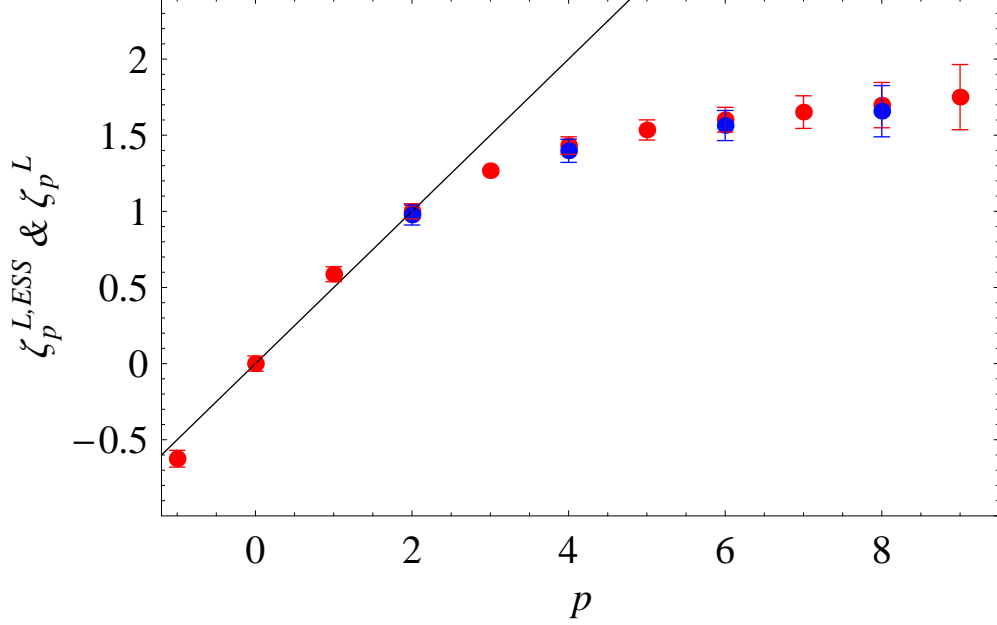


FIG. 11: Lagrangian anomalous scaling exponents ζ_p^L (blue curve) and the Extended self-similarity anomalous scaling exponents $\zeta_p^{L,ESS}$ (red curve). The straight line is the K41 prediction.

deduced from the Navier-Stokes equation. By plotting absolute (defined by positive velocity increments) structure functions vs. the third order structure function (Eulerian frame) or the second order structure function (Lagrangian frame), an extended scaling range can be observed because undulations in the structure functions are correlated and hence disappear when plotted against each other. ESS is widely used and gives seemingly universal scaling exponents for flows in a wide range of Reynolds numbers. As pointed out by Arneodo et al. [1] no consensus besides the observed facts exists about the interpretation or even significance of ESS. Whether the observed scaling in ESS is the signature of hidden physical laws is speculated. In the Lagrangian frame an additional problem arise. As already mentioned K41 predicts linear dependence of time scale for the Lagrangian second order structure function and hence $\zeta_2^L = 1$. This is motivated by the scaling in the Eulerian frame and specifically from the *four-fifth* law. A similar *exact* result does not exist for the Lagrangian structure functions. So all in all, one could state that *it is a wonder that it works!*

The values in Table II are in excellent agreement with results obtained by Xu et al. [34] and Mordant et al. [18]. The values by Biferale et al. [5] are somehow higher and was by Xu et al. [33] explained as a different choice of inertial range.

B. The multifractal framework

The multifractal model of turbulence was introduced by Parisi and Frisch [23] in the Eulerian frame after an early attempt by Mandelbrot [15] who used multifractal measures to characterize the spatial structure of dissipation in turbulence.

The multifractal model is phenomenological and has been able to successfully predict the corrections to K41 similarity scaling for high order moments of spatial velocity increments [11, 16, 30].

Borgas [8] discusses multifractals in the Lagrangian frame and introduces a bridge to the Eulerian framework. The literature is, however, not very rich on work on Lagrangian multifractals, which could have to do with the difficulties in obtaining reliable Lagrangian data set more than a animosity against the multifractal model. Work by Biferale et al. [5, 7], Chevillard et al. [10], Mordant et al. [17, 18], Xu et al. [34] have, however, shed light on the issue of multifractals in the Lagrangian frame.

In the Lagrangian multifractal model the flow is assumed to possess a range of scaling exponents h_{min}, \dots, h_{max} with a certain probability so that

$$\delta v(\tau) \sim \tau^h. \quad (12)$$

For each scaling exponent h there is a fractal set with a h -dependent dimension $D^L(h)$. The embedding dimension is one ($\tau \in \mathcal{R}$) and hence $D^L(h) \leq 1$ for all h . The probability $P_h^L(\tau)$ of having an exponent h at time τ is therefore proportional to $1 - D^L(h)$. From a steepest descent argument one can calculate a relation between the anomalous scaling exponents ζ_p^L and the fractal dimension $D^L(h)$ given by [11]:

$$\zeta_p^L = \inf_h [ph + 1 - D^L(h)]. \quad (13)$$

If $D^L(h)$ is *concave* a Legendre transformation gives

$$D^L(h) = \inf_p [ph + 1 - \zeta_p^L]. \quad (14)$$

In Figure 12 we have plotted $D^L(h)$ obtained through eqn. 14. First we calculated ζ_p^L for both integer and non-integer values of p between $p = -1$ and $p = 9$. The result is the red curve in the Figure 12.

The black dots are the result by Xu et al. [33] who in a PTV experiment of Reynolds number $Re_\lambda = 200, 690$ and 815 measured $D^L(h)$ both through $P_h^L(\tau)$ which they manage

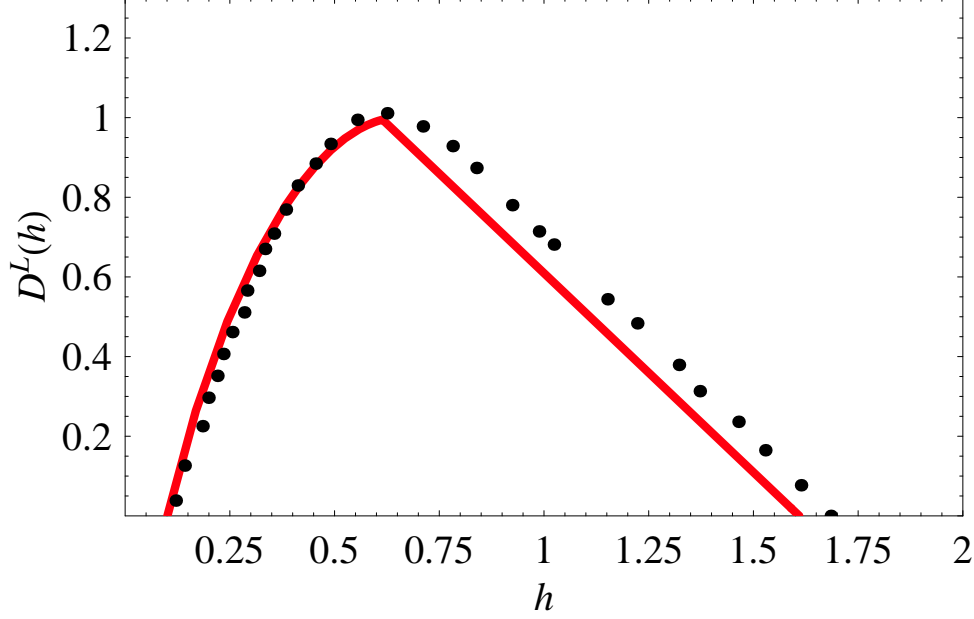


FIG. 12: The Lagrangian multifractal dimension spectrum $D^L(h)$. The black dots are the result by Xu et al. [33].

to measure directly and through eqn. 14 as we have done here. They arrived at the same $D^L(h)$ from both calculations putting confidence in the multifractal model for Lagrangian velocity increments. The agreement between their data and ours is very good. Only for $h > 0.6$ in the linear portion of $D^L(h)$ do we observe a discrepancy.

This linear portion of $D^L(h)$ was by Xu et al. [33] explained in the following way: because the domain of h is finite eqn. 13 will become a linear function after some p' . This linear behavior is also observed in Figure 11 for large ps . The transition point h' happens where p' minimizes the right hand side of eqn. 13. For $p > p'$ we therefore have that $\zeta_p^L = h_{min}p + 1$. Since only moments of the structure functions of order larger than -1 converge we have $p' = -1$ and the linear part of the curve is $D^L(h) = -h + 1 - \zeta_{-1}$. Xu et al. [33] successfully corrected the models by Biferale et al. [5] (from a theoretical prediction by She and Leveque [27]) and Chevillard et al. [10] and found a remarkable match. The discrepancy in Figure 12 therefore stems from different estimates of ζ_{-1}^L and the uncertainty in measuring it.

Chevillard et al. [10] came up with a formula for the connection between $D^L(h)$ and its Eulerian counterpart $D^E(h)$. The formula is

$$D^L(h) = -h + (1 + h) \left(D^E \left(\frac{h}{1 + h} \right) - 2 \right). \quad (15)$$

From our database we have calculated the Eulerian anomalous scaling exponents from ESS structure functions

$$S_{E,ESS}^p(r) \equiv \langle |\delta_r u(r)|^p \rangle \sim \langle |\delta_r u(r)|^3 \rangle^{\zeta_p^{E,ESS}}. \quad (16)$$

Results are shown in Figure 13. In (a) $S_{E,ESS}^p(r)$ are plotted from $p = 1, \dots, 9$. For all orders ESS seems to work fine. In (b) the anomalous scaling exponents $\zeta_p^{E,ESS}$ are shown.

The values are in perfect agreement with the theoretical model by She and Leveque [27]. More interesting is the departure from the K41 prediction which is smaller than in the Lagrangian frame. This is interpreted as Lagrangian statistics being more intermittent.

Just like in the Lagrangian frame there is a Legendre transformation between ζ_p^E and $D^E(h)$:

$$D^E(h) = \inf_p [ph + 3 - \zeta_p^E] \quad (17)$$

The only difference from eqn. 14 is the embedding dimension which in the Eulerian frame is three ($\mathbf{r} \in \mathcal{R}^3$).

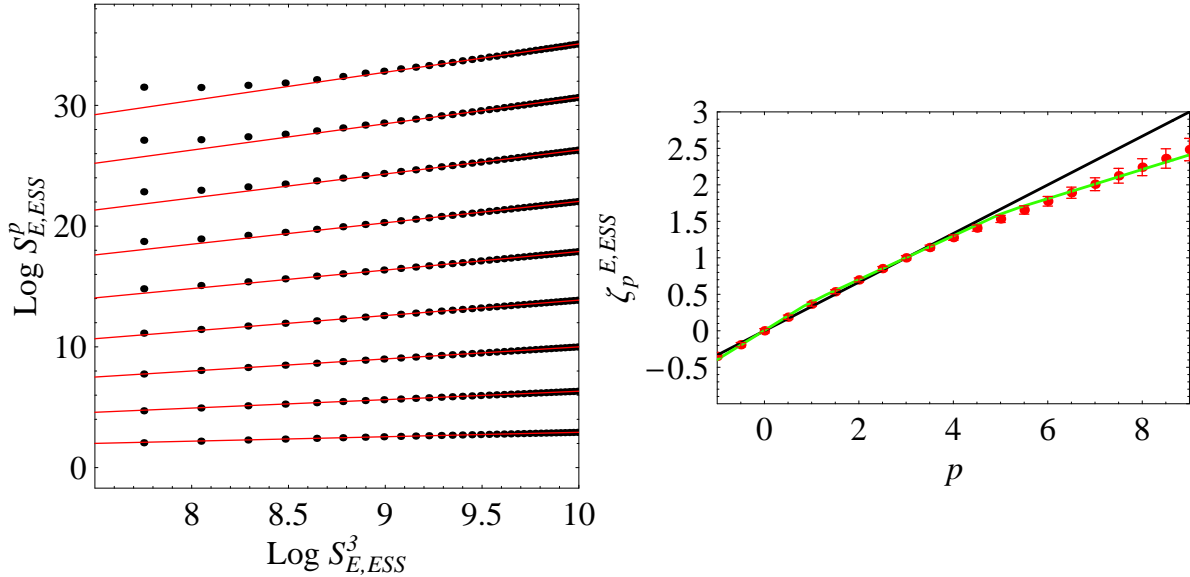


FIG. 13: (a) ESS Eulerian structure functions $S_{E,ESS}^p(r)$ of order p as a function of $S_{E,ESS}^3(r)$. $p = 1, \dots, 9$ increasing upwards. (b) Anomalous scaling exponent determined from (a) (red dots). The straight line is the K41 prediction and the green curve is the theoretical model by She and Leveque [27].

From eqn. 17 and 15 we can find $D^L(h)$ from the Eulerian anomalous scaling exponent presented in Figure 13 (b). The comparison is plotted in Figure 14. Again we observe

a discrepancy in the linear part of D_h^L . Whether it comes from the determination of the anomalous scaling exponents from ESS or that there is a flaw in eqn. 15 we can not say at the moment. A direct measurement of the probability P_h in both the Eulerian and Lagrangian frame might give more insight into the connection between the two frames.

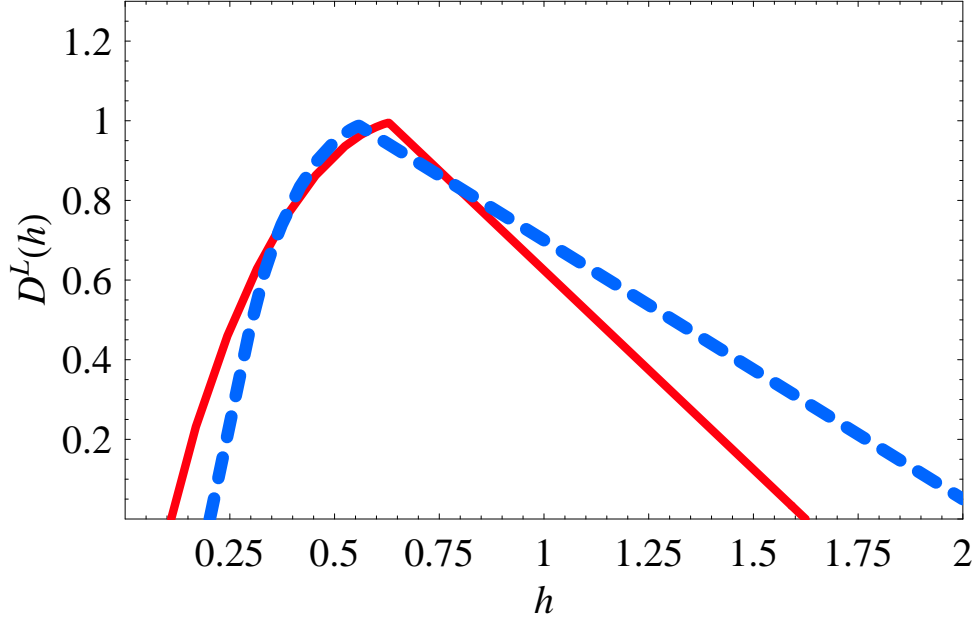


FIG. 14: The Lagrangian multifractal dimension spectrum $D(h)$. The red curve is calculated from Lagrangian ESS structure functions while the blue is obtained through Eulerian structure functions and 15.

The physical interpretation of the multifractal model is not that easy. In K41 similarity scaling only one scaling exponent is possible, namely $h = 1/3$ and thus $\zeta_p^E = p/3$. This is motivated from the fact the Navier-Stokes (N-S) equation is only invariant under one scaling group. This group is characterized by an exponent \bar{h} obtained by scaling the N-S with the following transformation (time, position, velocity): $t, \mathbf{r}, \mathbf{u} \mapsto \lambda^{1-\bar{h}}t, \lambda\mathbf{r}, \lambda^{\bar{h}}\mathbf{u}$ for $\lambda \in \mathcal{R}_+$. The solution is $\bar{h} = -1$. In the limit of infinite Reynolds number the viscosity term in the N-S equation becomes negligible and we find that the N-S equation is now invariant to infinitely many exponents \bar{h} . This is one of the motivations for the multifractal model. It is, however, not a justification. Another important aspect of the model is the fact that when an eddy breaks up into smaller eddies in the Richardson picture the smaller eddies do not cover the same amount of space. Instead they cover only a fraction equal to $3 - D^E(h)$. We thus have regions in the flow with large activity and regions with almost calm waters. In the

Lagrangian frame this would mean that the individual fluid particles are *not free* to move around in all directions. For example as reported by [24] and [7] are particles often trapped by intense vortices. The large accelerations and velocity increments of these events are therefore of dimension lower than 3 in the Eulerian frame and lower than 1 in the temporal. This spiral motion of fluid particle around a fluid filament is also the fluid mechanical picture of intermittent events in the model by She and Leveque [27]: by entraining surrounding fluid kinetic energy fluctuations are effectively dissipated along the axis of the filament.

As emphasized by Borgas [8] the multifractal model does, however, not imply that the trajectories of fluid particles are fractal trajectories themselves.

V. CONCLUSIONS

We have measured Lagrangian one-particle statistics and looked at small-scale behavior. The finiteness of the measuring volume can be used to calculate the mean kinetic energy dissipation ε in the flow without any further assumptions. The small scales do seem to be affected by the large-scale inhomogeneities present in our flow. We do not observe a significant inertial range but by Extended Self-Similarity we are able to extract a quantitative measure of the structure functions of high order. From these we calculate the Lagrangian anomalous scaling exponents and find excellent agreement with already published results.

Via the multifractal model we have calculated the Lagrangian multifractal dimension spectrum. The spectrum is similar to the one published by Xu et al. [34] even though our Reynolds number is significantly lower and our mean flow is different.

Most importantly we have shown that a high Reynolds number is not necessary to obtain results in the Lagrangian frame. All experiments and DNS do show the same qualitative features and no clear Lagrangian inertial range has been observed. Whether it is because current experiments are performed with too low Reynolds number or it simply do not exist future experiments will tell.

Acknowledgments

The author is grateful to Beat Lüthi, Søren Ott and Jakob Mann.

- [1] A. Arneodo, C. Baudet, F. Belin, R. Benzi, B. Castaing, B. Chabaud, R. Chavarria, S. Ciliberto, R. Camussi, F. Chilla, B. Dubrulle, Y. Gagne, B. Hebral, J. Herweijer, M. Marchand, J. Maurer, J. F. Muzy, A. Naert, A. Noullez, J. Peinke, F. Roux, P. Tabeling, W. Van de Water, and H. Willaime. Structure functions in turbulence, in various flow configurations, at reynolds number between 30 and 5000 using extended self-similarity. *Europhys. Lett.*, 34:411, 1996.
- [2] R. Benzi, S. Ciliberto, R. Tripiccone, C. Baudet, and S. Succi. Extended self-similarity in turbulent flow. *Phys. Rev. E.*, 48:29, 1993.
- [3] J. Berg, B. Lüthi, J. Mann, and S. Ott. Backwards and forwards relative dispersion in turbulent flow: An experimental investigation. *Phys. Rev. E*, 34:115, 2006.
- [4] J. Berg, B. Lüthi, S. Ott, and J. Mann. Coarse-grained strain dynamics and backwards/forwards dispersion. *manuscript in preparation*, 2006.
- [5] L. Biferale, G. Boffetta, A. Celani, B. J. Devenish, A. Lanotte, and F. Toschi. Multifractal statistics of lagrangian velocity and acceleration in turbulence. *Phys. Rev. Lett.*, 93:064502, 2004.
- [6] L. Biferale, G. Boffetta, A. Celani, B. J. Devenish, A. Lanotte, and F. Toschi. Multiparticle dispersion in fully developed turbulence. *Phys. Fluids.*, 17:111701, 2005.
- [7] L. Biferale, G. Boffetta, A. Celani, B. J. Devenish, A. Lanotte, and F. Toschi. Particle trapping in three-dimensional fully developed turbulence. *Phys. Fluids*, 17:021701, 2005.
- [8] M. A. Borgas. The multifractal lagrangian nature of turbulence. *Phil. Trans. R. Soc. Lond. A.*, 342:379, 1993.
- [9] M. Bourgoïn, N. T. Ouellette, H. Xu, J. Berg, and E. Bodenschatz. The role of pair dispersion in turbulent flow. *Science*, 311:835, 2006.
- [10] L. Chevillard, S. G. Roux, E. L  v  que, N. Mordant, J.-F. Pinton, and A. Arneodo. Lagrangian velocity statistics in turbulent flow: effects of dissipation. *Phys. Rev. Lett.*, 91:214502, 2003.
- [11] U. Frisch. *Turbulence – the legacy of A. N. Kolmogorov*. Cambridge, 1995.

- [12] R.-C. Lien and E. A. D’Asaro. The kolmogorov constant for the lagrangian velocity spectrum and structure function. *Phys. Fluids.*, 14:4456, 2002.
- [13] B. Lüthi, A. Tsinober, and W. Kinzelbach. Lagrangian measurements of vorticity dynamics in turbulent flow. *J. Fluid Mech.*, 528:87, 2005.
- [14] B. Lüthi, J. Berg, S. Ott, and Mann J. Lagrangian multi-particle statistics. *submitted*, 2006.
- [15] B. B. Mandelbrot. Intermittent turbulence in self-similar cascades: divergence of high moments and dimension of the carrier. *J. Fluid Mech.*, 62:331, 1975.
- [16] C. Meneveau, K. R. Sreenivasan, P. Kailanath, and M. S. Fan. Joint multifractal measures: Theory and applications to turbulence. *Phys. Rev. A*, 41:894, 1990.
- [17] N. Mordant, J. Delour, E. Lévêque, A. Arnéodo, and J.-F. Pinton. Long time correlatios in lagrangian dynamics: a key to intermittency in turbulence. *Phys. Rev. Lett.*, 89:254502, 2002.
- [18] N. Mordant, E. Lévêque, and J.-F. Pinton. Experimental and numerical study of the lagrangian dynamics of high Reynolds turbulence. *New. J. Phys.*, 6:116, 2004.
- [19] N. Mordant, P. Metz, O. Michel, and J.-F. Pinton. Mearesurement of lagrangian velocity in fully developed turbulence. *Phys. Rev. Lett.*, 87:214501, 2001.
- [20] S. Ott and J. Mann. An experimental investigation of the relative diffusion of particle pairs in three-dimensional flow. *J. Fluid Mech.*, 422:207, 2000.
- [21] N. T. Ouellette, H. Xu, and E. Bodenschatz. A quantitative study of three-dimensional lagrangian particle tracking algorithms. *Exp. in Fluids.*, 40:301, 2006.
- [22] N. T. Ouellette, H. Xu, M. Bourgoïn, and E. Bodenschatz. Small-scale anisotropy in lagrangian turbulence. *New. J. Phys.*, 8:102, 2006.
- [23] G. Parisi and U. Frisch. On the singularity structure of fully developed turbulence. *Turbulence and predictability in geophysical fluid dynamics, Proceed. Intern. School of Physics ‘E. Fermi’, 1983, Varenna, Italy 84-87, eds. M. Ghil, R. Benzi and G. Parisi. North Holland, Amsterdam.*
- [24] A. La Porta, G. A. Voth, J. Alexander A. M. Crawford, and E. Bodenschatz. Fluid particle accelerations in fully developed turbulence. *Nature*, 409:1017, 2001.
- [25] B. Sawford. Reynolds number effects in lagrangian stochastic models of turbulent dispersion. *Phys. Fluids A*, 3:1577, 1991.
- [26] B. Sawford. Turbulent relative dispersion. *Annu. Rev. Fluid Mech.*, 422:207, 2001.
- [27] Z.-S. She and E. Leveque. Universal scaling laws in fully developed turbulence. *Phys. Rev. Lett.*, 72:336, 1994.

- [28] X. Shen and Z. Warhaft. The anisotropy of the small scale structure in high Reynolds number ($Re_\lambda \sim 1000$) turbulent shear flow. *Phys. Fluids*, 12:2976, 2000.
- [29] X. Shen and Z. Warhaft. Longitudinal and transverse structure functions in sheared and unsheared wind-tunnel turbulence. *Phys. Fluids*, 14:370, 2002.
- [30] K. R. Sreenivasan and R. A. Antonia. The phenomenological of small-scale turbulence. *Annu. Rev. Fluid Mech.*, 29:435, 1997.
- [31] H. Tennekes and J. L. Lumley. *A first course in turbulence*. MIT Press, 1972.
- [32] J. Willneff. *A spatio-temporal matching algorithm for 3D-particle tracking velocimetry*. PhD thesis, ETH Zürich, 2003.
- [33] H. Xu, M. Bourgoïn, N. T. Ouellette, and E. Bodenschatz. High order lagrangian velocity statistics in turbulence. *Phys. Rev. Lett.*, 96:024503, 2006.
- [34] H. Xu, N. T. Ouellette, and E. Bodenschatz. Multifractal dimension of lagrangian turbulence. *Phys. Rev. Lett.*, 96:114503, 2006.
- [35] P. K. Yeung. Lagrangian investigations of turbulence. *Annu. Rev. Fluid Mech.*, 34:115, 2002.